One-Step Synthesis of High Entropy Oxide Supported Rhodium Catalyst for Highly Selective CO Production in CO₂ Hydrogenation

Siyuan Zhu¹, Yufeng Chen¹, Vasishta Somayaji¹, Peter Novello¹, Dennis Chacko², Fanxing Li², Jie Liu^{1*}

KEYWORDS: High entropy oxide, CO₂ hydrogenation, Strong metal-support interaction, One-step synthesis, Rhodium-based catalyst.

ABSTRACT: High entropy oxide (HEO) has shown to be a new type of catalyst support with tunable composition-function properties for many chemical reactions. However, the preparation of metal nanoparticle catalyst supported on metal oxide support is time-consuming and takes multiple complicated steps. Herein, we used a one-step glycine-nitrate-based combustion method to synthesize highly dispersed rhodium nanoparticles on a high surface area high entropy oxide. This catalyst shows a high selectivity to produce CO in CO₂ hydrogenation with 80% higher activity compared to rhodium nanoparticle-based catalysts. We've also studied the effect of different metal elements in HEO and demonstrated that high CO selectivity is achieved if one of the metals in the metal oxide support favors CO production. We identified that copper and zinc are responsible for the observed high CO selectivity due to their low *CO binding strength. During hydrogenation, a strong metal-support interaction (SMSI) was created through charge transfer and formed an encapsulated structure between rhodium nanoparticles and HEO support to lower the *CO binding strength, which enables high CO selectivity in the reaction. By combining different metal oxide into high entropy oxide as a catalyst support, high activity and high selectivity can be achieved at the same time in the CO₂ hydrogenation reaction.

INTRODUCTION

Heterogeneous catalysis is the dominating process in the current chemical industry, such as the Fischer-Tropsch synthesis, ammonia synthesis, biomass conversion, selective oxidation, and others^{1, 2}. Over the years, metal nanoparticles catalyst is becoming the main choice in heterogenous catalysis, but it requires a support, such as metal oxide with high specific surface areas, porosities, and thermal and mechanical stability, to stabilize the nanoparticles and provide an environment to maximize the catalyst activity of the nanoparticles^{2, 3}. The general synthesis methods of supported nanoparticle catalysts include precipitation, impregnation and drying, and other emerging techniques, such as melt infiltration, colloidal synthesis and atomic layer deposition (ALD)², which requires multiple steps. New methods that can produce these catalysts in a more economical and simple manner is desired by the society.

In this work, we choose to study the solid-gas phase CO₂ hydrogenation reaction in order to suppress the emission of CO₂ and convert it to useful chemicals⁴. Under the ambient pressure, CO and CH₄ are the products through reverse water-gas shift (RWSG) reaction and methanation reaction. It is important that the selectivity can be tuned to produce CO, because it can be readily converted, along with H₂, to lower olefins, gasoline diesel, wax and oxygenates in Fischer-Tropsch synthesis⁵. Various metal (Cu^{6, 7}, Pd⁸, Pt⁹, Rh¹⁰, and Ni¹¹) and metal oxide (TiO₂ ^{6, 9, 10}, ZrO₂^{6, 11}, Al₂O₃⁷, CeO₂^{8, 11}) combination has been reported to actively produce CO in the CO₂ hydrogenation reaction. In these reactions, *CO is an important intermediate in the CO₂ hydrogenation

reaction¹². The binding strength between *CO and metal/oxide interface dominates whether it primarily produce CO or further hydrogenated to CH₄⁴. It was discovered in 1978 that strong metal-support interaction (SMSI) can be induced by reducing noble metals supported on TiO2 to decrease the adsorption energy of CO and H₂¹³. In CO₂ hydrogenation, SMSI can lower the adsorption energy of *CO and form the encapsulated structure to block the CO₂ methanation active sites to achieve desirable high CO selectivity¹⁴⁻¹⁸. Reducible metal oxides, such as CeO₂, MoO₃ and ZrO₂, are used to form SMSI^{14, 19}. SMSI can also be enhanced by changing the crystal structure of the supports^{15, 16}, and photochemistry method through UV irradiation¹⁸. The particle size as well as metal loading could also affect the activity and selectivity by forming more active sites and more encapsulated structures through SMSI¹⁹.

Recently, a new class of materials, high entropy material (HEMs), has emerged as a novel catalyst for HER²⁰, OER^{21, 22}, ORR^{23, 24}, and CO₂ conversion reactions²⁵⁻²⁷. One specific type of HEMs, High entropy oxide (HEO), has recently been applied in the fields of thermal, electro- and photo- catalysis²⁸⁻³², and used as catalyst support to stabilize single atom catalysts or nanoparticles^{26, 33, 34}. However, the reported mechanochemical synthesis method needs to use ball milling for 2 hours to achieve single phase HEO crystal or followed by adding noble metal precursor and calcinating at high temperature^{33, 34}. Herein, we designed a novel, easy, and one-step synthesis method for synthesizing highly dispersive rhodium nanoparticles on HEO support using the glycinenitrate combustion method, which was used for synthesizing oxide ceramic powder and first reported in 1990³⁵. A single-

¹Department of Chemistry, Duke University, Durham, NC 27708

²Department of Chemical and Biomolecular Engineering, North Carolina State University, Raleigh, NC 27695

phase high entropy oxide was synthesized immediately after evaporating all water, and then combustion happened. Adding rhodium nanoparticles on high entropy oxide could also be integrated into the combustion process and achieve onestep synthesis simultaneously by adding rhodium precursor to the aqueous solution. The obtained catalyst exhibits high catalytic performance and highly selective CO production in CO₂ hydrogenation reaction. We also discovered that copper and zinc are the two key elements in the HEO support that contributes to high CO selectivity. We conclude that the combined high catalytic performance and highly selective CO production comes from the synergy with the catalytic HEO support and strong metal-support interaction with the HEO support by forming encapsulated structure and lowering *CO binding strength under the CO₂ hydrogenation reaction conditions.

RESULTS AND DISCUSSION

The synthesis of high entropy oxide is by a combustion method using nitrate salts as precursor in aqueous solution (as shown in Scheme 1). After evaporating all water and getting a slurry, violent combustion (Figure 1a) happened in the round bottom flask. A uniform powder sample was collected and washed with deionized water to remove all organic residue and salts. X-ray diffraction (XRD) pattern in Figure 1b demonstrated that a single-phase rock salt high entropy oxide was formed after combustion. The HAADF images and EDS mapping with 50nm scale bar showed all six elements (O, Mg, Co, Ni, Cu, Zn) were well distributed in high entropy oxide. It also indicated that the combustion method is successful in synthesizing high entropy oxide in a fast single-step process.

To use this high entropy oxide as catalyst support, two methods were used to introduce rhodium on the high entropy oxide support. First, rhodium nanoparticle was synthesized on high entropy oxide support by a wet impregnation method using rhodium chloride as precursor followed by hydrogen reduction in a tube furnace at 400°C for 2 hrs, which is named as Rh-w/HEO. Second, Rh catalyst supported on HEO were produced by directly adding Rh precursor (rhodium chloride) into the HEO precursor mixture before the combustion process (as shown in scheme 1). Samples prepared using this method were named as Rh-c/HEO. Under the HAADF images and rhodium mapping (Figure 2b and 2c), the rhodium nanoparticles with size of 10nm (Figure S1) were well dispersed on the high entropy oxide by using glycine-nitrate combustion (Rh-c/HEO, figure 2b). However, the rhodium nanoparticles synthesized by wet-impregnation (Rh-w/HEO, figure 2c) were easier to aggregate together, and formed some 20nm clusters on the HEO support. All six elements were well dispersed in HEO support for Rh-c/HEO. However, on Rh-w/HEO, there were a few spots that cobalt and copper were aggregated due to the hydrogen reduction in the synthesis. X-ray diffraction (XRD) pattern was performed to compare the crystal structure of HEO and rhodium in different samples (as shown in figure 2a). The HEO has

three major peaks at 36.6°, 42,6° 61.9°, which attribute to (111), (200), (220) planes of the cubic rock salt structure. The other two small peaks at 74.1° and 77.1° are from (311) and (222) planes. When the rhodium nanoparticles were added on HEO by wet impregnation method (Rh-w/HEO), the peak position of (111) (200), and (220) is the same, indicating that the HEO crystal structure remains same after adding rhodium nanoparticles on it. When using glycine-nitrate combustion method to add rhodium on HEO (Rh-c/HEO), all the peak shifts to large numbers by 0.2°, which are at 36.8°, 42.8° and 62.1°. This indicates that rhodium had strong interaction with HEO, which led to a smaller lattice distortion. The X-ray photoelectron spectroscopy (XPS) was used to measure the oxidation state of rhodium nanoparticles on HEO, As shown in Figure S2, rhodium 3d_{5/2} has a 310.3eV binding energy, which is higher than Rh metal (307.6eV) and Rh native oxide (308.8eV). This further demonstrates that rhodium had strong interaction with HEO support. The Rh-O, Rh-metal, Rh-O-metal binding causes that rhodium $3d_{5/2}$ has a broad peak with high binding energy. Due to the combustion in the air. Rh-c/HEO had a stronger peak at 35.6° than Rh-w/HEO, which was attributed to rhodium oxide. Rh-w/HEO had another small peak at 38.9°, which can be attributed to CuO (111) plane.

To test the catalytic performance of these two catalysts which have the same composition (5wt% Rh on HEO) but different structures through different synthesis methods, the reactor setup as shown in Figure 3a has been used. Two thermocouples were used to measure the catalyst top temperature as T1 and the catalyst bottom temperature as T2. T2 was used as the set temperature for all measurements. In the CO₂ hydrogenation reaction, both CH₄ and CO were detected as products. The Rh-c/HEO is a more active catalyst compared to Rh-w/HEO in CO₂ hydrogenation reaction for producing both CO and CH₄ (as shown in Figure 3b and 3c). The production rate increased exponentially when the set temperature increased from 200°C to 500°C. At 500°C, the CO production rate of Rh-c/HEO can reach 100.2 µmol/g s, which is 63.2% higher than Rh-w/HEO (61.4 µmol/g s). The CH₄ production rate of Rh-c/HEO is 1.7 µmol/g s at 500°C, which is almost 7 times higher than the Rh-w/HEO production rate (0.25µmol/g s). It can demonstrate that highly dispersive rhodium nanoparticles on HEO synthesized by combustion method have more active sites compared to using wet-impregnation method putting rhodium nanoparticles on HEO with the same weight ratio (5%).

To study how the composition of the HEO supports affect the selectivity in CO₂ hydrogenation reaction, rhodium nanoparticles supported on single element metal oxide supports were synthesized using the same glycine-nitrate synthesis method, and the rhodium weight ratio is controlled at around 5%, verified by EDS (Figure S5 and Table S1). As shown in Figure 4a, all catalysts with rhodium on metal oxides support can produce CO. Among them, the catalyst on NiO support has the highest CO production rate. It reaches the highest production rate at 475°C with an 87.0 μmol/g s CO production rate. The other four metal oxide supports reach the highest production rate at 500°C. The highest CO

production rates are 64.3 µmol/g s, 58.3 µmol/g s, 48.2 μmol/g s, and 41.4 μmol/g s for catalysts supported on MgO, CoO, ZnO, and CuO at 500C, respectively. For CH₄ production as shown in Figure 4b, NiO, MgO, and CoO are still the same metal oxides support and have the highest production rates. The CH₄ production rate reaches 60.8 µmol/g s, 42.7 umol/g s, and 40.8 umol/g s at 500°C, respectively. For CuO and ZnO metal oxide supports, the CH₄ production rate is substantially lower compared to the other three metal oxide supports and their own CO production rate. It can only reach 0.17 µmol/g s and 0.20 µmol/g s respectively. Therefore, rhodium on CuO or ZnO has an over 99% CO selectivity in CO₂ selectivity. But for NiO, MgO, and CoO, both CO and CH₄ were produced. As the CH₄ production rates increase exponentially faster than the CO production rate, the CH₄ selectivity increases as the temperature increases (as shown in Figure 4c). The CH₄ selectivity reaches 41.8%, 39.9%, and 41.2% for NiO, MgO, and CoO, respectively, which turns to 58.2%, 60.1%, and 58.8% CO selectivity.

After discovering that CuO and ZnO are two metal oxide supports that initiate high CO selectivity in CO₂ hydrogenation, while NiO, MgO, and CoO are metal oxide supports that can produce both CO and CH₄. Further experiments have been performed to understand and explain high entropy oxide with 5 elements enables high CO selectivity while maintaining high reactivity. First, using the same glycinenitrate combustion to synthesize rhodium on the tri-metal oxide support, (MgCoNi)O with the same 5% rhodium weight ratio, verified by EDS (Figure S5 and Table S1). Since all the single metal oxides can produce both CO and CH₄ and they favor producing more CH₄ as temperature increases, when mixing three metal oxides together, the CH₄ selectivity increases to 65.7% at 500°C as shown in Figure 4d. Then, Cu was added to synthesize rhodium on quadmetal oxides (MgCoNiCu)O with the same synthesis method and same rhodium ratio. As shown in Figure 4d, the CO selectivity was enhanced from 34.3% to 87.0% after CuO was added to (MgCoNi)O, and CO selectivity can be further enhanced to 99% after ZnO was added as a high entropy oxide support. It demonstrates that CuO and ZnO are the two key factors for high CO selectivity in HEO catalyst support. The CO₂ hydrogenation reaction pathway will change from CH₄ to CO if CuO or ZnO exist in the metal oxide catalyst support. However, if Cu and Zn were the only component of metal oxide support, the CO selectivity can still be over 99%, but the CO production rate was only 29.2 μmol/g s, less than 30% of Rh-c/HEO (Figure S6a and S6b).

To study the surface chemistry and interaction between rhodium catalyst and metal oxide catalyst support, the XPS of the original catalyst and the catalyst reduced by H_2 in a tube furnace at 500°C was studied. Since the Mg auger electron spectrum overlaps with Rh 3d orbital energy under monochromated Al K α (1486.7eV) X-ray source, two of the samples, Rh-c/HEO and Rh/MgO, were measured using a lower X-ray energy source (Mg K α , 1253.6eV). However, the lower X-ray energy source resulted in a lower resolution in the spectrum. Since the samples only contained around 5% Rh, it resulted in the fact that Rh peak was not observed in

the survey. Therefore, in Table S2, only four samples that didn't contain Mg were included. For all the samples, the atomic ratio between rhodium and metallic elements in metal oxide decreased after H2 treatment. Among these four samples, Rh/NiO had the largest decrease (from 0.84 to 0.037), and the highest CO production rate as shown in Fig 3(a). The Rh/CoO had a medium production rate, and it had a 64% decrease in the ratio (from 0.35 to 0.127). The Rh/CuO and Rh/ZnO had the two lowest CO production rates, it only having a 38% (from 0.23 to 0.142) and 21% (0.231 to 0,186) decrease in the ratios, respectively. Since XPS is a surface sensitive method, and its sensitivity is dependent on the kinetic energy of Rh 3d electrons and their inelastic mean free path (IMFP) and effective attenuation length (EAL). IMFP is defined as average distance that an electron with an given energy can travel, and EAL is considered for the application of measurement of overlayer-film thickness³⁶. Herein, we used NIST standard reference database to calculate the IMFP of Rh before H2 treatment, and EAL after H₂ treatment and the SMSI layer is formed^{37, 38}. The IMFPs of Rh are estimated as 1.348nm under Al Kα (1486.7eV) X-ray source, or 1.591nm under Mg Ka (1253.6eV) X-ray source. However, the EALs of Mg, Co, Ni, Cu, Zn on Rh are estimated as 0.55Å, 0.315Å, 0.303Å. 0.328Å, 0.363Å, respectively. The SMSI formed by reduced layer is one to two atomic layer thick. Therefore, the estimated EALs are close to the SMSI layer thickness³⁹. The decrease in the ratio between Rh and other metal elements is an indication of the formation of embedded Rh structures on the catalyst surface. The degree of the decrease of this ratio had an inverse relationship with the CO production rate. which indicates that the more rhodium embedded structures formed, the higher CO it could produce. The SMSI layer formed by reducible metal oxide support is the key to high CO production rate. This phenomena was observed by other groups in in situ XPS that Ru/Mo surface ratio decrease when the reduction temperature increase, which was explained as the graduate encapsulation by metal oxide support¹⁴. As shown in Figure 5a and b, in high resolution STEM image and HAADF mode, there was an amorphous SMSI layer on the crystallized Rh nanoparticle for the used Rh-c/HEO catalysts. This is direct evidence shown that SMSI was formed during the CO₂ hydrogenation reaction. The thickness of SMSI layer varied from 0.46 Å to 1.3 nm, which matched the XPS penetration depth. Co, Ni, Cu has been reported as catalyst CO₂ hydrogenation reaction⁴⁰⁻⁴². For the used Rh-c/HEO catalysts, under the reduced condition, Co, Ni, Cu had a few bright spots shown in EDS mapping (Figure S8), which indicated some nanoparticles and clusters were formed on HEO support. The Cu and Zn mappings were closer to O mapping compared to Mg, Co, Ni. In the XRD pattern, the single-phase crystal peaks were split into 2 peaks for the used catalysts (Figure S9). The Cu and Zn formed its own binary metal oxide. HEO could also be the catalyst support itself, which contributed to around 30% CO production here (Figure S10a). But adding rhodium would also decrease the methane production rate to 30% of the pure HEO at 500°C (Figure S10b). The methane production on HEO was prevented with Rh added. The high CO production rate and high selectivity comes from synergy of highly well dispersed rhodium nanoparticles from combustion, SMSI layer formed by H₂ reduction, and catalytic high entropy oxide support. Even though, HEO support could be reduced during the CO₂ hydrogenation reaction and crystal structure would become different (Figure S9 and S10), the CO production rate of Rh-c/HEO can remain stable for 100 hours (Figure S11)

To understand the high CO selectivity from CuO and ZnO, we compared Rh 3d_{5/2} XPS spectra for all five single metal oxide support (Figure 5). Rh exists in either a metallic state (lower binding energy), or an oxidized state (higher binding energy). It can be seen that metallic Rh in CuO and ZnO had lower binding energy, 306.24 eV and 306.46 eV respectively compared to other metal oxides and the calibration standard (307.6 eV). With strong metal-support interaction (SMSI), the decrease of metallic Rh binding energy could come from electron charge transfer from the metal oxide support with the additional valence electron charge. Therefore, Rh had stronger SMSI with CuO and ZnO compared to other metal oxide supports, which limited the CH₄ production.

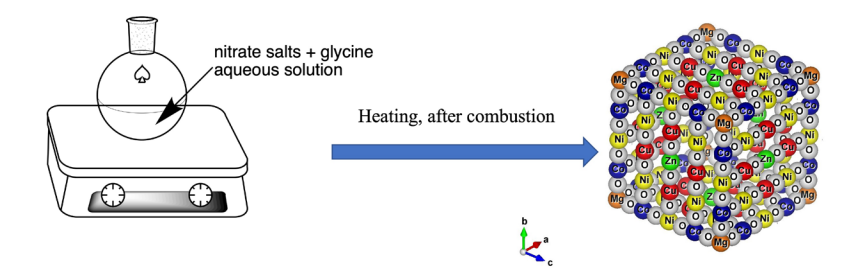
To further study the *CO binding strength affected by the composition of catalyst support, in situ diffuse-reflectance infrared Fourier transform spectroscopy (DRIFTS) was used to study the reaction intermediates and molecules adsorbed on the catalyst surface at 500°C during the CO₂ hydrogenation reaction. As shown in Figure 6, all the catalysts showed a strong CO₂ binding peak from 2300 cm⁻¹ to 2380 cm⁻¹, which corresponds to the reaction results that all catalysts are active in the CO₂ hydrogenation reaction. Both Rh/MgO and Rh/(MgCoNi)O show a *CO binding peak at 2040 cm⁻ 1, but the *CO binding peak was not detected on Rh-c/HEO and Rh/(MgCoNiCu)O. This further demonstrated that the overall *CO binding strength can be lowered by adding Cu and Zn into metal oxide support. The binding strength of *CO on the catalyst is a crucial factor to control the selectivity in CO₂ hydrogenation reaction⁴. Weaker *CO binding strength favors higher CO selectivity due to faster desorption of *CO, and a strong *CO binding strength is an indication of lower CO selectivity due to further dissociation to *C and *O and subsequent hydrogenation to CH₄¹². Therefore, the DRIFTS results indicate that Cu and Zn are two key elements in high entropy oxide support that are responsible to the high CO selectivity by lowing the *CO binding strength at the metal/oxide interface. Without Cu and Zn in the metal oxide support composition (Rh/(MgCoNi)O), the CO selectivity was only 34%. With Cu adding to the composion, the *CO binding strength was weakened, the CO selectivity was enhanced to 87%. With Zn adding to form high entropy oxide, the *CO binding strength was further weakened, the overall 99% selectivity was achieved (Figure 4d).

In the high entropy support composition, Mg, Co and Ni were responsible for forming more Rh embedded SMSI structure for high CO production, Cu and Zn were responsible for weakening *CO binding strength for high CO selectivity. The synergy between rhodium nanoparticle and high entropy oxide, and each element in the high entropy oxide support made this catalyst having the both highest activity and CO selectivity among all rhodium-based catalysts reported in the literatures (Table S3)

CONCULSION

Using one-step glycine-nitrate combustion method to synthesize rhodium nanoparticles on high entropy oxide, small size rhodium nanoparticles can be well dispersed on high entropy oxide support making it easier to form a strong metal-support interaction. The HEO metal oxide support has 99% CO selectivity and highest CO production activity in the CO₂ hydrogenation reaction compared to other single metal oxide supports. Within the HEO, Cu and Zn are the two key elements that could form a stronger metal-support interaction with rhodium than Mg, Co, Ni, which lowers the *CO binding strength to enable high CO selectivity in the CO₂ hydrogenation reaction. Overall, by combing metal oxides in the form of HEO, highly selective CO production with high catalytic activity can be achieved simultaneously, demonstrating the advantage of HEO as a versatile catalyst support in heterogeneous catalysis.

Figures and Captions:



Scheme 1 One step synthesis of high entropy oxide (MgCoNiCuZn)O

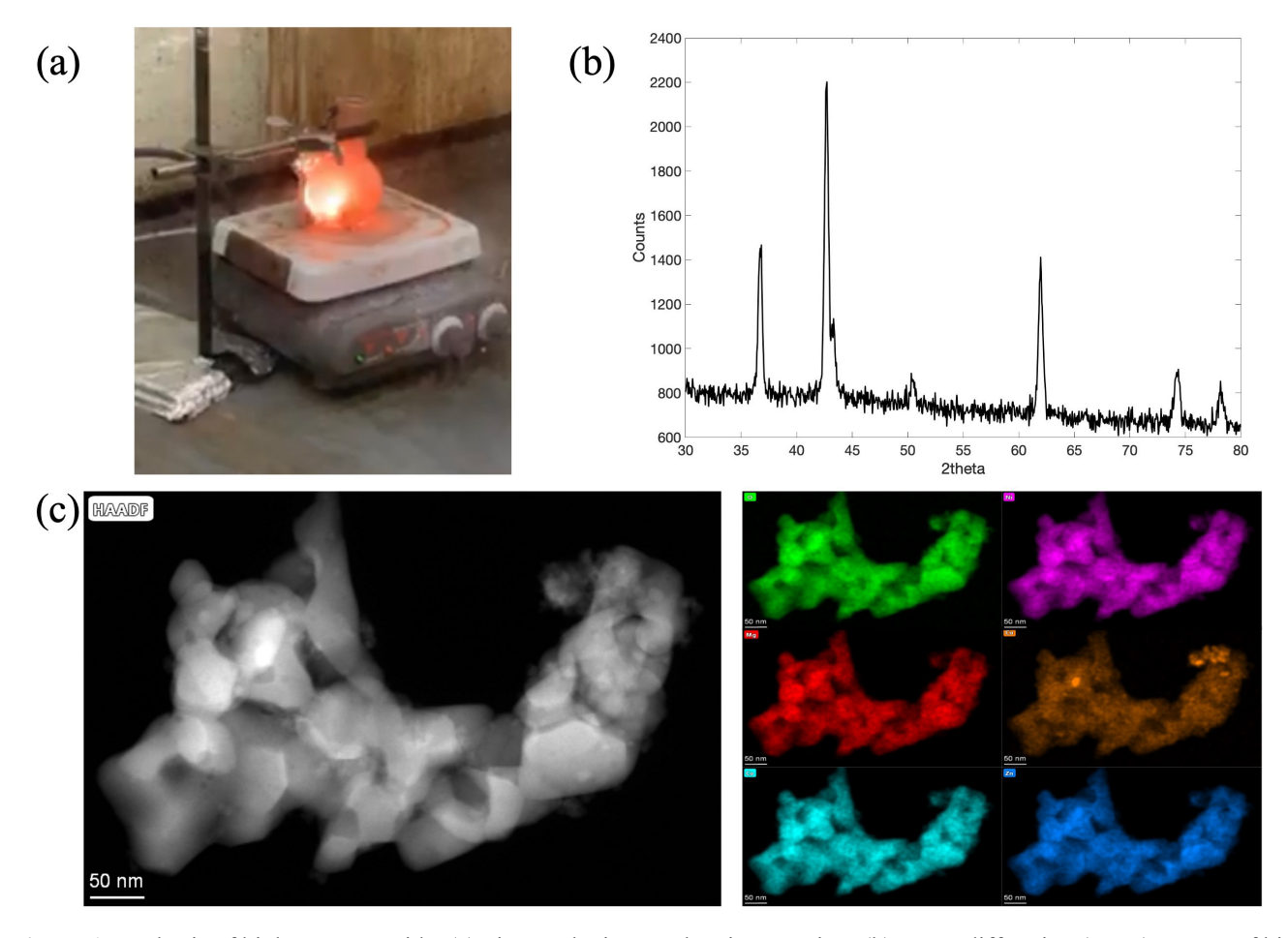


Figure 1 Synthesis of high entropy oxide. (a) nitrate-glycine combustion reaction; (b) X-ray diffraction (XRD) pattern of high entropy oxide; (c) High-angle annular dark-field (HADDF) images and energy dispersive X-ray analysis (EDS) mappings of high entropy oxide.

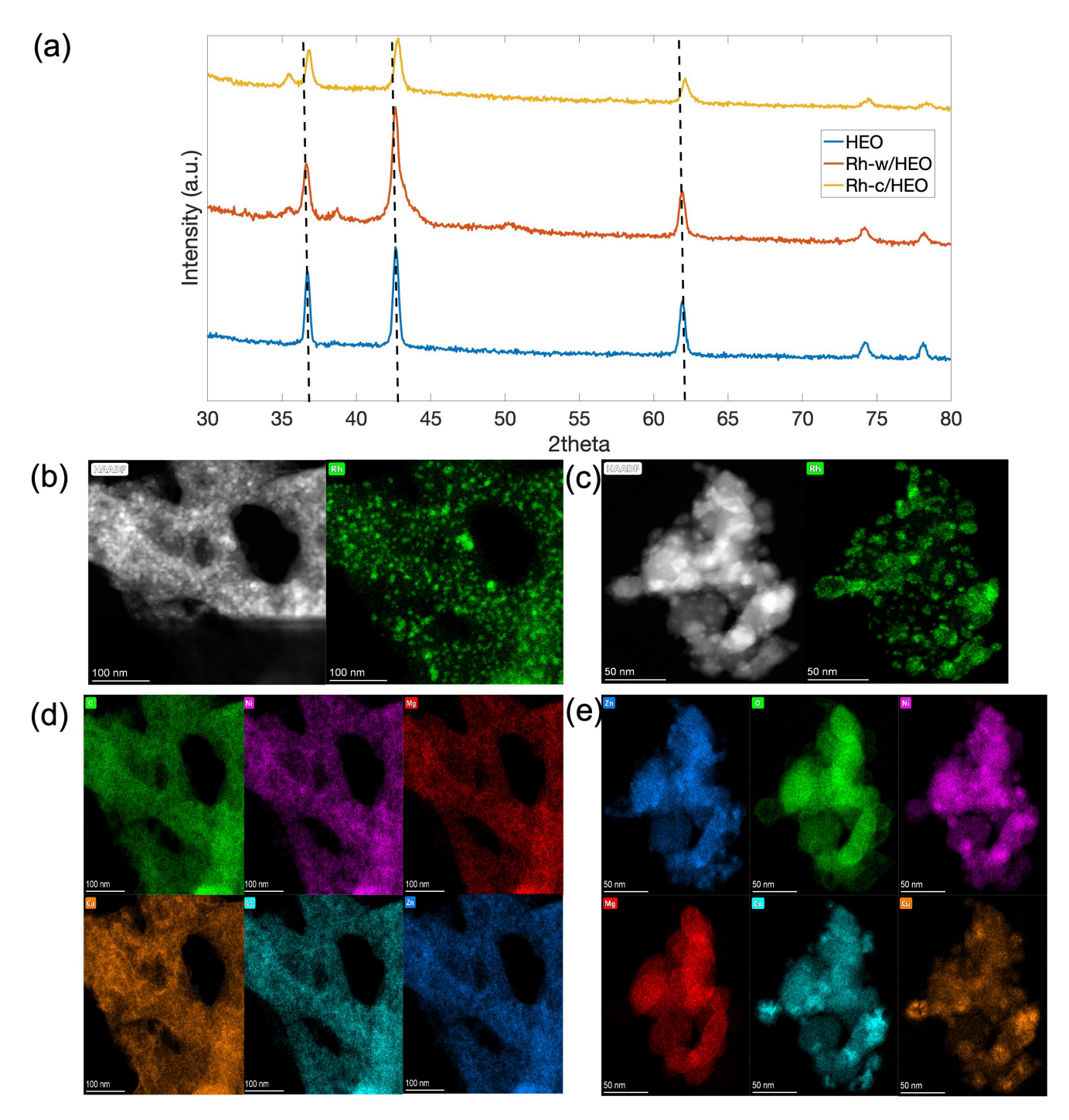


Figure 2 (a) X-ray diffraction patterns for high entropy oxide, HEO (blue curve), Rh-w/HEO (red curve), and Rh-c/HEO (yellow curve); (b) HAADF image and rhodium mapping of Rh-w/HEO by wet-impregnation synthesis method; (c) HAADF image and rhodium mapping of Rh-c/HEO by glycine-nitrate combustion synthesis method; (d) EDS mapping of high entropy oxide of Rh-c/HEO; (e) EDS mapping of high entropy oxide of Rh-w/HEO

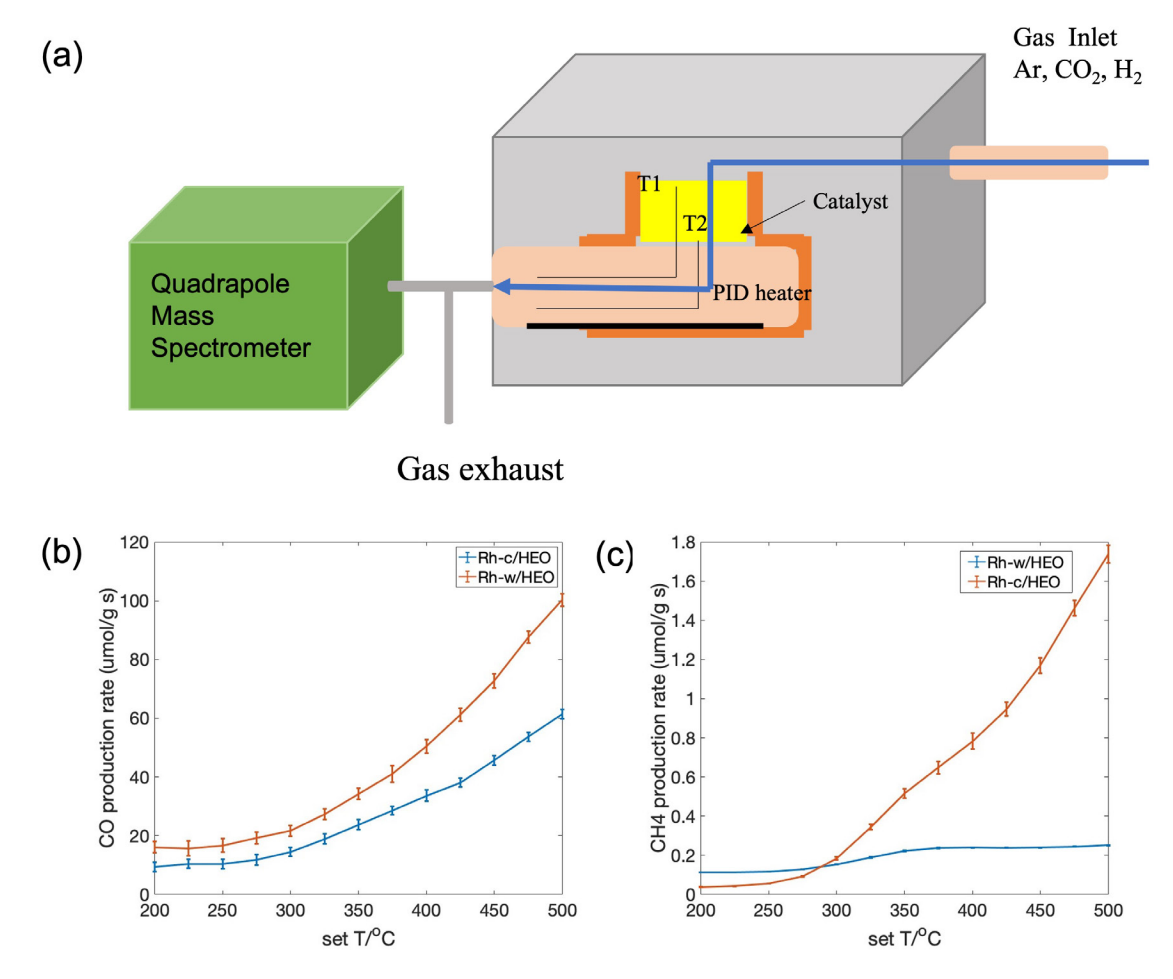


Figure 3 (a) CO₂ hydrogenation solid-gas phase reaction system set-up; (b) Measured CO production rate, wet-impregnation method, Rh-w/HEO (blue curve), glycine-nitrate combustion method, Rh-c/HEO (red curve); (c) Measured CH₄ production rate, wet-impregnation method, Rh-w/HEO (blue curve), glycine-nitrate combustion method, Rh-c/HEO (red curve)

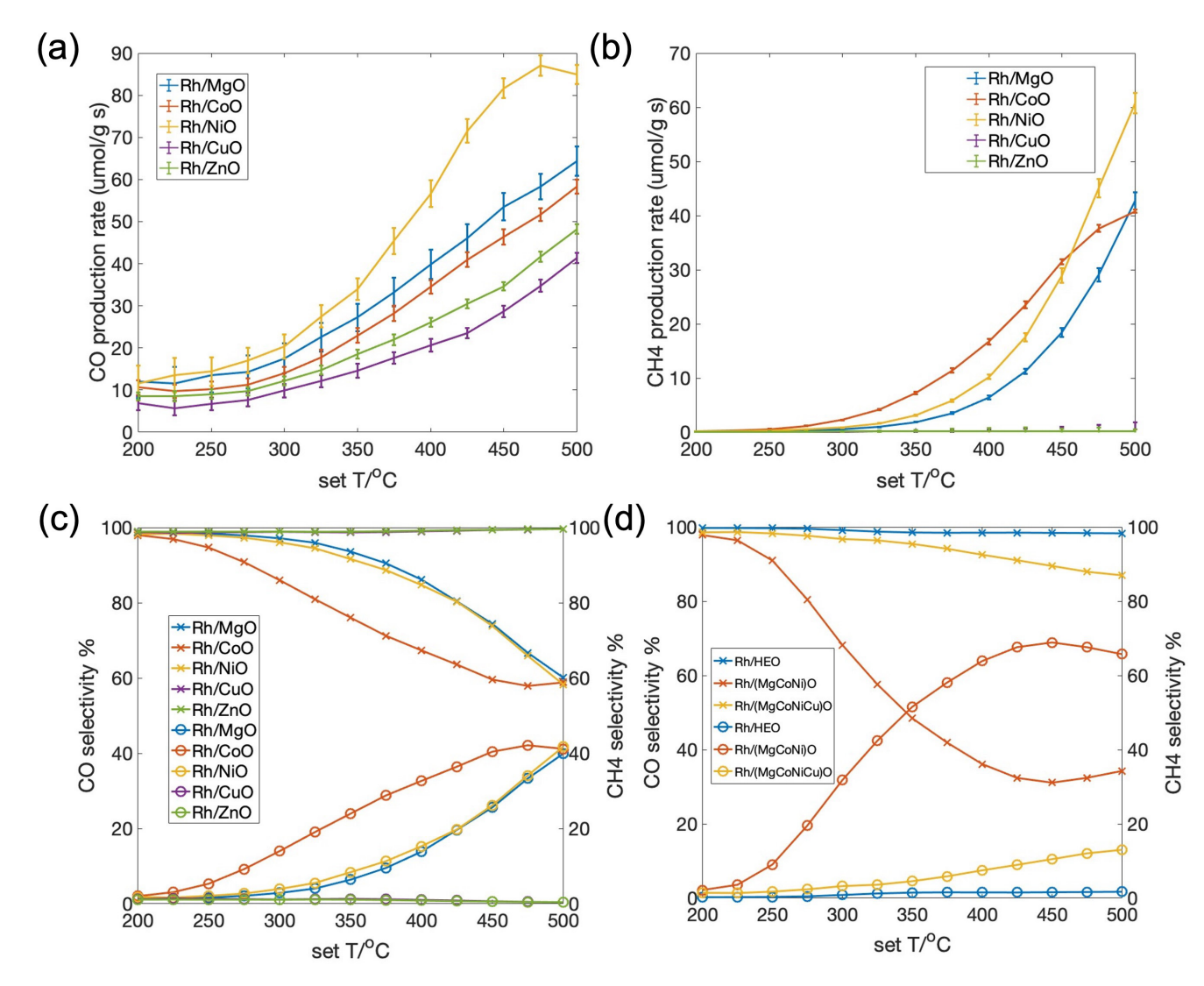


Figure 4 (a) Measured CO production rate, Rh/MgO (blue curve), Rh/CoO (red curve), Rh/NiO (yellow curve), Rh/CuO (purple curve), Rh/ZnO (green curve); (b) Measured CH₄ production rate, Rh/MgO (blue curve), Rh/CoO (red curve), Rh/NiO (yellow curve), Rh/CuO (purple curve), Rh/ZnO (green curve); (c) Calculated CO and CH₄ selectivity, symbol 'x' corresponds to the CO selectivity on left y axis, symbol 'o' corresponds to the CH₄ on right y axis, Rh/MgO (blue curve), Rh/CoO (red curve), Rh/NiO (yellow curve), Rh/CuO (purple curve), Rh/ZnO (green curve); (d) Calculated CO and CH₄ selectivity, symbol 'x' corresponds to the CO selectivity on left y axis, symbol 'o' corresponds to the CH₄ on right y axis, Rh/HEO (blue curve), Rh/(MgCoNiO) (red curve), Rh/(MgCoNiCu)O (yellow curve).

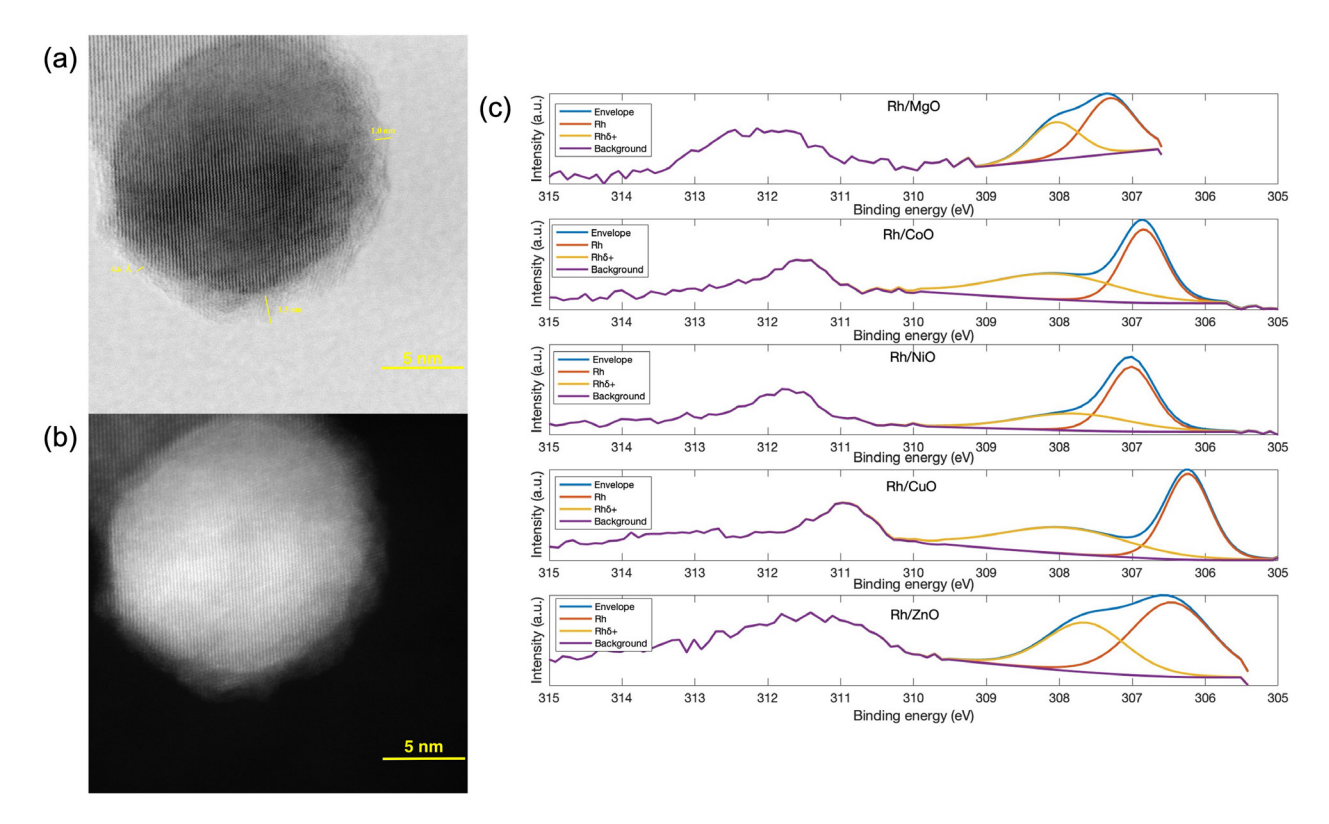
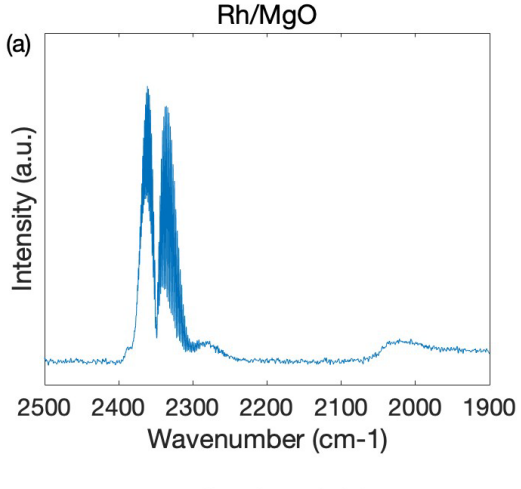
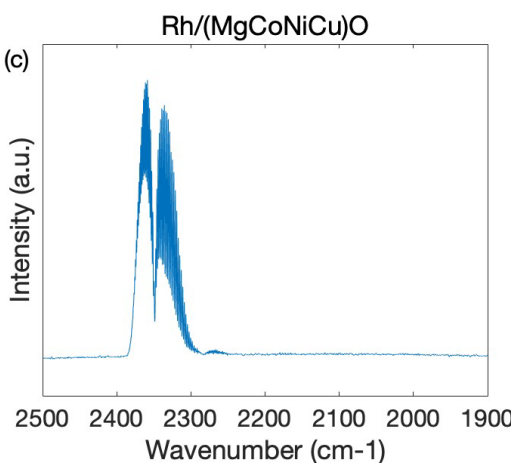
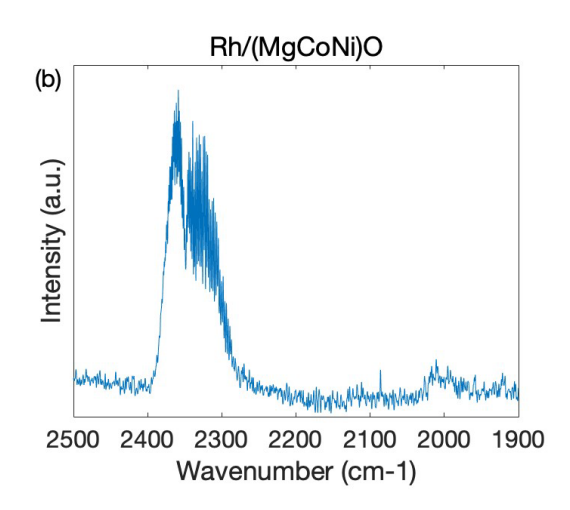


Figure 5. (a) High resolution STEM image for used Rh-c/HEO catalysts; (b) High resolution STEM image in HAADF mode for used Rh-c/HEO catalysts; (c)Rh $3d_{5/2}$ XPS spectra from all five single metal oxide catalysts. Envelope (blue curve), Rh⁰ (red curve), Rh^{δ +} (yellow curve), background (purple curve).







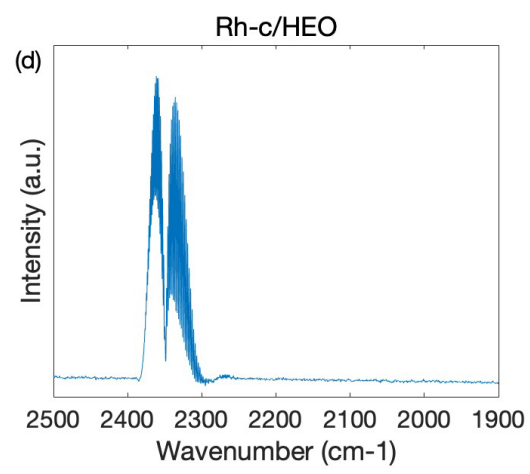


Figure 6. in situ DRIFTS spectra of (a) Rh/MgO, (b) Rh/(MgCoNi)O, (c) Rh/(MgCoNiCu)O and (d) Rh-c/HEO

ASSOCIATED CONTENT

Supporting Information

The Supporting Information is available free of charge on the ACS Publications website.

Detailed experiment section includes catalyst preparation, reactor setup and CO₂ hydrogenation reaction, materials characterization, inelastic mean free pathway (IMFP) and effective attenuation length (EAL) calculation, *in-situ* diffuse reflectance infrared Fourier transformation spectroscopy (DRIFTS). Additional figures and tables.

AUTHOR INFORMATION

Corresponding Author

Jie Liu - Department of Chemistry, Duke University, Durham, NC 27708; email: j.liu@duke.edu

Authors

Siyuan Zhu - Department of Chemistry, Duke University, Durham, NC 27708; email: siyuan.zhu@duke.edu

Yufeng Chen – Department of Chemistry, Duke University, Durham, NC 27708; email: yufeng.chen@duke.edu

Vasishta Somayaji - Department of Chemistry, Duke University, Durham, NC 27708; email: vasishta.somayaji@duke.edu

Peter Novello - Department of Chemistry, Duke University, Durham, NC 27708; email: peter.novello@duke.edu

Dennis Chacko - Department of Chemical and Biomolecular Engineeering, North Carolina State University, Raleigh, NC 27695; email: dchacko@ncsu.edu

Faxing Li - Department of Chemical and Biomolecular Engineeering, North Carolina State University, Raleigh, NC 27695; email: fli5@ncsu.edu

Author Contributions

The manuscript was written through contributions of all authors. All authors have given approval to the final version of the manuscript. S.Z and J.L. designed this research. S.Z. synthesized all catalysts and performed all tests. P.N. set up the reactor and wrote the LabVIEW program to control the reactor. D.C. and F.L.

performed *in situ* DRIFTS. Y.C. set up the reactor and gas system to prepare used catalyst for further characterization. V.S. prepared the XRD and STEM samples for used catalysts. S.Z. wrote the draft. J.L. revised the draft and submitted it.

Funding Sources

NSF: CHE-1954838.

ACKNOWLEDGMENT

This research was supported in part by the National Science Foundation (grant number CHE-1954838). The authors also acknowledge support by the Duke University Shared Materials Instrumentation Facility (SMIF), a member of the North Carolina Research Triangle Nanotechnology Network (RTNN), which is supported by the National Science Foundation (Grant ECCS-1542015) as part of the National Nanotechnology Coordinated Infrastructure (NNCI). This work was also performed in part at the Analytical Instrumentation Facility (AIF) at North Carolina State University, which is supported by the State of North Carolina and the National Science Foundation (award number ECCS-2025064). The AIF is a member of the North Carolina Research Triangle Nanotechnology Network (RTNN), a site in the National Nanotechnology Coordinated Infrastructure (NNCI).

REFERENCES

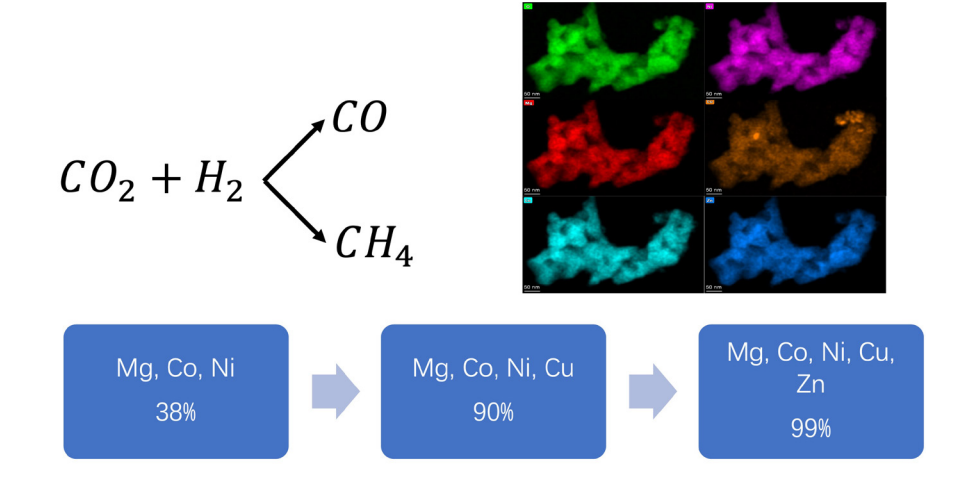
- (1) Friend, C. M.; Xu, B. Heterogeneous Catalysis: A Central Science for a Sustainable Future. *Accounts of Chemical Research* **2017**, *50* (3), 517-521. DOI: 10.1021/acs.accounts.6b00510.
- (2) Munnik, P.; de Jongh, P. E.; de Jong, K. P. Recent Developments in the Synthesis of Supported Catalysts. *Chemical Reviews* **2015**, *115* (14), 6687-6718. DOI: 10.1021/cr500486u.
- (3) Astruc, D. Introduction: Nanoparticles in Catalysis. *Chemical Reviews* **2020**, *120* (2), 461-463. DOI:
- 10.1021/acs.chemrev.8b00696.
- (4) Wang, L.-X.; Wang, L.; Xiao, F.-S. Tuning product selectivity in CO2 hydrogenation over metal-based catalysts. *Chemical Science* **2021**, *12* (44), 14660-14673, 10.1039/D1SC03109K. DOI: 10.1039/D1SC03109K.
- (5) Chen, Y.; Wei, J.; Duyar, M. S.; Ordomsky, V. V.; Khodakov, A. Y.; Liu, J. Carbon-based catalysts for Fischer–Tropsch synthesis. *Chemical Society Reviews* **2021**, *50* (4), 2337-2366, 10.1039/D0CS00905A. DOI: 10.1039/D0CS00905A.
- (6) Kattel, S.; Yan, B.; Yang, Y.; Chen, J. G.; Liu, P. Optimizing Binding Energies of Key Intermediates for CO2 Hydrogenation to Methanol over Oxide-Supported Copper. *Journal of the American Chemical Society* **2016**, *138* (38), 12440-12450. DOI: 10.1021/jacs.6b05791.
- (7) Wang, J. B.; Lee, H.-K.; Huang, T.-J. Synergistic Catalysis of Carbon Dioxide Hydrogenation into Methanol by Yttria-Doped Ceria/γ-Alumina-Supported Copper Oxide Catalysts: Effect of Support and Dopant. *Catalysis Letters* **2002**, *83* (1), 79-86. DOI: 10.1023/A:1020613700495.
- (8) Fan, L.; Fujimoto, K. Development of an active and stable ceria-supported palladium catalyst for hydrogenation of carbon dioxide to methanol. *Applied Catalysis A: General* **1993**, *106* (1), L1-L7. DOI: https://doi.org/10.1016/0926-860X(93)80152-G.
- (9) Kattel, S.; Yan, B.; Chen, J. G.; Liu, P. CO2 hydrogenation on Pt, Pt/SiO2 and Pt/TiO2: Importance of synergy between Pt and oxide support. *Journal of Catalysis* **2016**, *343*, 115-126. DOI: https://doi.org/10.1016/j.jcat.2015.12.019.
- (10) Gogate, M. R.; Davis, R. J. Comparative study of CO and CO2 hydrogenation over supported Rh–Fe catalysts. *Catalysis Communications* **2010**, *11* (10), 901-906. DOI: https://doi.org/10.1016/j.catcom.2010.03.020.

- (11) Aldana, P. A. U.; Ocampo, F.; Kobl, K.; Louis, B.; Thibault-Starzyk, F.; Daturi, M.; Bazin, P.; Thomas, S.; Roger, A. C. Catalytic CO2 valorization into CH4 on Ni-based ceria-zirconia. Reaction mechanism by operando IR spectroscopy. *Catalysis Today* **2013**, *215*, 201-207. DOI: https://doi.org/10.1016/j.cattod.2013.02.019.
- (12) Kattel, S.; Liu, P.; Chen, J. G. Tuning Selectivity of CO2 Hydrogenation Reactions at the Metal/Oxide Interface. *Journal of the American Chemical Society* **2017**, *139* (29), 9739-9754. DOI: 10.1021/jacs.7b05362.
- (13) Tauster, S. J.; Fung, S. C.; Garten, R. L. Strong metal-support interactions. Group 8 noble metals supported on titanium dioxide. *Journal of the American Chemical Society* **1978**, *100* (1), 170-175. DOI: 10.1021/ja00469a029.
- (14) Xin, H.; Lin, L.; Li, R.; Li, D.; Song, T.; Mu, R.; Fu, Q.; Bao, X. Overturning CO2 Hydrogenation Selectivity with High Activity via Reaction-Induced Strong Metal—Support Interactions. *Journal of the American Chemical Society* **2022**, *144* (11), 4874-4882. DOI: 10.1021/jacs.1c12603.
- (15) Li, X.; Lin, J.; Li, L.; Huang, Y.; Pan, X.; Collins, S. E.; Ren, Y.; Su, Y.; Kang, L.; Liu, X.; et al. Controlling CO2 Hydrogenation Selectivity by Metal-Supported Electron Transfer. *Angewandte Chemie International Edition* **2020**, *59* (45), 19983-19989. DOI: https://doi.org/10.1002/anie.202003847.
- (16) Li, W.; Zhang, G.; Jiang, X.; Liu, Y.; Zhu, J.; Ding, F.; Liu, Z.; Guo, X.; Song, C. CO2 Hydrogenation on Unpromoted and M-Promoted Co/TiO2 Catalysts (M = Zr, K, Cs): Effects of Crystal Phase of Supports and Metal–Support Interaction on Tuning Product Distribution. *ACS Catalysis* **2019**, *9* (4), 2739-2751. DOI: 10.1021/acscatal.8b04720.
- (17) Matsubu, J. C.; Zhang, S.; DeRita, L.; Marinkovic, N. S.; Chen, J. G.; Graham, G. W.; Pan, X.; Christopher, P. Adsorbate-mediated strong metal–support interactions in oxide-supported Rh catalysts. *Nature Chemistry* **2017**, *9* (2), 120-127. DOI: 10.1038/nchem.2607.
- (18) Chen, H.; Yang, Z.; Wang, X.; Polo-Garzon, F.; Halstenberg, P. W.; Wang, T.; Suo, X.; Yang, S.-Z.; Meyer, H. M.; Wu, Z.; et al. Photoinduced Strong Metal—Support Interaction for Enhanced Catalysis. *Journal of the American Chemical Society* **2021**, *143* (23), 8521-8526. DOI: 10.1021/jacs.0c12817.
- (19) Wang, Y.; Winter, L. R.; Chen, J. G.; Yan, B. CO2 hydrogenation over heterogeneous catalysts at atmospheric pressure: from electronic properties to product selectivity. *Green Chemistry* **2021**, *23* (1), 249-267, 10.1039/D0GC03506H. DOI: 10.1039/D0GC03506H.
- (20) Zhang, G.; Ming, K.; Kang, J.; Huang, Q.; Zhang, Z.; Zheng, X.; Bi, X. High entropy alloy as a highly active and stable electrocatalyst for hydrogen evolution reaction. *Electrochimica Acta* **2018**, *279*, 19-23. DOI:
- https://doi.org/10.1016/j.electacta.2018.05.035.
- (21) Wang, D.; Liu, Z.; Du, S.; Zhang, Y.; Li, H.; Xiao, Z.; Chen, W.; Chen, R.; Wang, Y.; Zou, Y.; et al. Low-temperature synthesis of small-sized high-entropy oxides for water oxidation. *Journal of Materials Chemistry A* **2019**, 7 (42), 24211-24216, 10.1039/C9TA08740K. DOI: 10.1039/C9TA08740K.
- (22) Qiu, H.-J.; Fang, G.; Gao, J.; Wen, Y.; Lv, J.; Li, H.; Xie, G.; Liu, X.; Sun, S. Noble Metal-Free Nanoporous High-Entropy Alloys as Highly Efficient Electrocatalysts for Oxygen Evolution Reaction. *ACS Materials Letters* **2019**, *1* (5), 526-533. DOI: 10.1021/acsmaterialslett.9b00414.
- (23) Chen, X.; Si, C.; Gao, Y.; Frenzel, J.; Sun, J.; Eggeler, G.; Zhang, Z. Multi-component nanoporous platinum—ruthenium—copper—osmium—iridium alloy with enhanced electrocatalytic activity towards methanol oxidation and oxygen reduction. *Journal of Power Sources* **2015**, *273*, 324-332. DOI: https://doi.org/10.1016/j.jpowsour.2014.09.076.

- (24) Jin, Z.; Lv, J.; Jia, H.; Liu, W.; Li, H.; Chen, Z.; Lin, X.; Xie, G.; Liu, X.; Sun, S.; et al. Nanoporous Al-Ni-Co-Ir-Mo High-Entropy Alloy for Record-High Water Splitting Activity in Acidic Environments. *Small* **2019**, *15* (47), 1904180. DOI: 10.1002/smll.201904180 (accessed 2020/01/12).
- (25) Pedersen, J. K.; Batchelor, T. A. A.; Bagger, A.; Rossmeisl, J. High-Entropy Alloys as Catalysts for the CO2 and CO Reduction Reactions. *ACS Catalysis* **2020**, *10* (3), 2169-2176. DOI: 10.1021/acscatal.9b04343.
- (26) Chen, H.; Lin, W.; Zhang, Z.; Jie, K.; Mullins, D. R.; Sang, X.; Yang, S.-Z.; Jafta, C. J.; Bridges, C. A.; Hu, X.; et al. Mechanochemical Synthesis of High Entropy Oxide Materials under Ambient Conditions: Dispersion of Catalysts via Entropy Maximization. *ACS Materials Letters* **2019**, *1* (1), 83-88. DOI: 10.1021/acsmaterialslett.9b00064.
- (27) Nellaiappan, S.; Katiyar, N. K.; Kumar, R.; Parui, A.; Malviya, K. D.; Pradeep, K. G.; Singh, A. K.; Sharma, S.; Tiwary, C. S.; Biswas, K. High-Entropy Alloys as Catalysts for the CO2 and CO Reduction Reactions: Experimental Realization. *ACS Catalysis* **2020**, *10* (6), 3658-3663. DOI: 10.1021/acscatal.9b04302.
- (28) Albedwawi, S. H.; AlJaberi, A.; Haidemenopoulos, G. N.; Polychronopoulou, K. High entropy oxides-exploring a paradigm of promising catalysts: A review. *Materials & Design* **2021**, *202*, 109534. DOI: https://doi.org/10.1016/j.matdes.2021.109534. (29) Gao, Y.; Liu, Y.; Yu, H.; Zou, D. High-entropy oxides for catalysis: Status and perspectives. *Applied Catalysis A: General* **2022**, *631*, 118478. DOI: https://doi.org/10.1016/j.apcata.2022.118478.
- (30) Riley, C.; De La Riva, A.; Park, J. E.; Percival, S. J.; Benavidez, A.; Coker, E. N.; Aidun, R. E.; Paisley, E. A.; Datye, A.; Chou, S. S. A High Entropy Oxide Designed to Catalyze CO Oxidation Without Precious Metals. *ACS Applied Materials & Interfaces* **2021**, *13* (7), 8120-8128. DOI: 10.1021/acsami.0c17446.
- (31) Edalati, P.; Wang, Q.; Razavi-Khosroshahi, H.; Fuji, M.; Ishihara, T.; Edalati, K. Photocatalytic hydrogen evolution on a high-entropy oxide. *Journal of Materials Chemistry A* **2020**, *8* (7), 3814-3821, 10.1039/C9TA12846H. DOI: 10.1039/C9TA12846H. (32) Nguyen, T. X.; Liao, Y.-C.; Lin, C.-C.; Su, Y.-H.; Ting, J.-M. Advanced High Entropy Perovskite Oxide Electrocatalyst for Oxygen Evolution Reaction. *Advanced Functional Materials* **2021**, *31* (27), 2101632. DOI: https://doi.org/10.1002/adfm.202101632.
- (33) Xu, H.; Zhang, Z.; Liu, J.; Do-Thanh, C.-L.; Chen, H.; Xu, S.; Lin, Q.; Jiao, Y.; Wang, J.; Wang, Y.; et al. Entropy-stabilized

- single-atom Pd catalysts via high-entropy fluorite oxide supports. *Nature Communications* **2020**, *11* (1), 3908. DOI: 10.1038/s41467-020-17738-9.
- (34) Chen, H.; Sun, Y.; Yang, S.; Wang, H.; Dmowski, W.; Egami, T.; Dai, S. Self-regenerative noble metal catalysts supported on high-entropy oxides. *Chemical Communications* **2020**, *56* (95), 15056-15059, 10.1039/D0CC05860B. DOI: 10.1039/D0CC05860B.
- (35) Chick, L. A.; Pederson, L. R.; Maupin, G. D.; Bates, J. L.; Thomas, L. E.; Exarhos, G. J. Glycine-nitrate combustion synthesis of oxide ceramic powders. *Materials Letters* **1990**, *10* (1), 6-12. DOI: https://doi.org/10.1016/0167-577X(90)90003-5. (36) Powell, C. J.; Jablonski, A. Surface sensitivity of X-ray photoelectron spectroscopy. *Nuclear Instruments and Methods in Physics Research Section A: Accelerators, Spectrometers, Detectors and Associated Equipment 2009, <i>601* (1), 54-65. DOI: https://doi.org/10.1016/j.nima.2008.12.103.
- (37) Jablonski, C. J. P. a. A. *NIST Electron Inelastic-Mean-Free-Path Database Version 1.2*; National Institute of Standards and Technology, 2010.
- (38) Jablonski, C. J. P. a. A. *NIST Electron Effective-Attenuation-Length Database Version 1.3*; National Institute of Standards and Technology, 2011.
- (39) Zhang, S.; Plessow, P. N.; Willis, J. J.; Dai, S.; Xu, M.; Graham, G. W.; Cargnello, M.; Abild-Pedersen, F.; Pan, X. Dynamical Observation and Detailed Description of Catalysts under Strong Metal–Support Interaction. *Nano Letters* **2016**, *16* (7), 4528-4534. DOI: 10.1021/acs.nanolett.6b01769.
- (40) Fan, T.; Liu, H.; Shao, S.; Gong, Y.; Li, G.; Tang, Z. Cobalt Catalysts Enable Selective Hydrogenation of CO2 toward Diverse Products: Recent Progress and Perspective. *The Journal of Physical Chemistry Letters* **2021**, *12* (43), 10486-10496. DOI: 10.1021/acs.jpclett.1c03043.
- (41) Lozano-Reis, P.; Prats, H.; Gamallo, P.; Illas, F.; Sayós, R. Multiscale Study of the Mechanism of Catalytic CO2 Hydrogenation: Role of the Ni(111) Facets. *ACS Catalysis* **2020**, *10* (15), 8077-8089. DOI: 10.1021/acscatal.0c01599.
- (42) Rui, N.; Shi, R.; Gutiérrez, R. A.; Rosales, R.; Kang, J.; Mahapatra, M.; Ramírez, P. J.; Senanayake, S. D.; Rodriguez, J. A. CO2 Hydrogenation on ZrO2/Cu(111) Surfaces: Production of Methane and Methanol. *Industrial & Engineering Chemistry Research* **2021**, *60* (51), 18900-18906. DOI: 10.1021/acs.iecr.1c03229.

Table of Contents/Abstract Graphics



Abstract

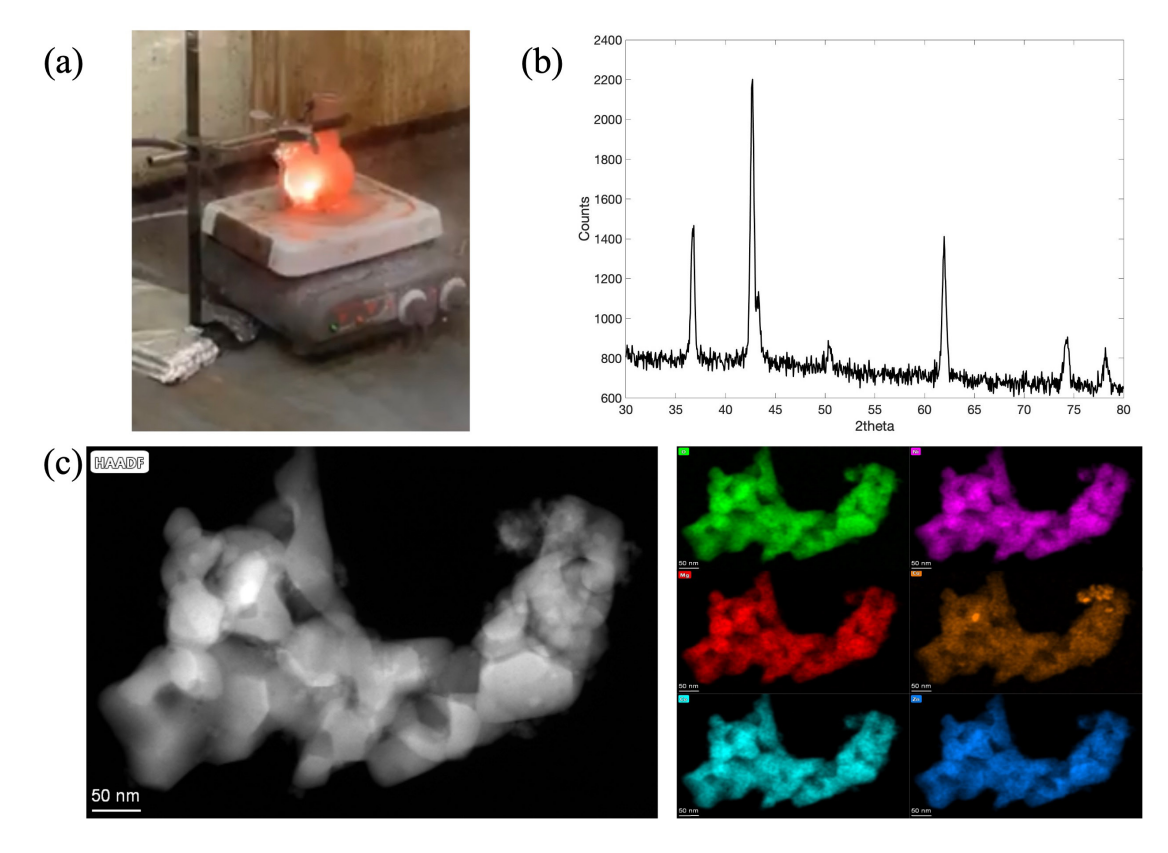


Figure 1: Synthesis of high entropy oxide. (a) nitrate-glycine combustion reaction; (b) X-ray diffraction (XRD) pattern of high entropy oxide; (c) High-angle annular dark-field (HADDF) images and energy dispersive X-ray analysis (EDS) mappings of high entropy oxide

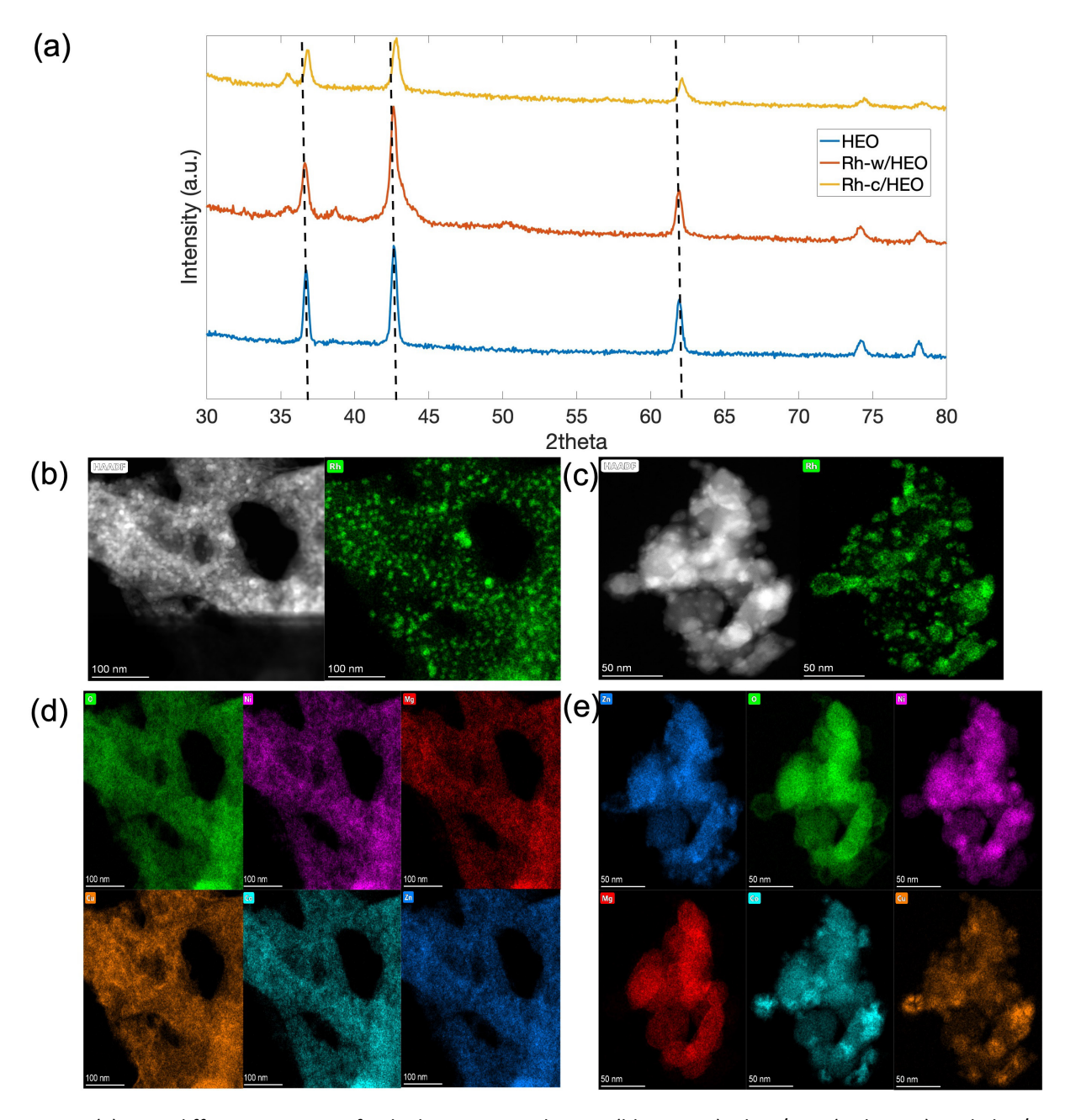


Figure 2: (a) X-ray diffraction patterns for high entropy oxide, HEO (blue curve), Rh-w/HEO (red curve), and Rh-c/HEO (yellow curve); (b) HAADF image and rhodium mapping of Rh-w/HEO by wet-impregnation synthesis method; (c) HAADF image and rhodium mapping of Rh

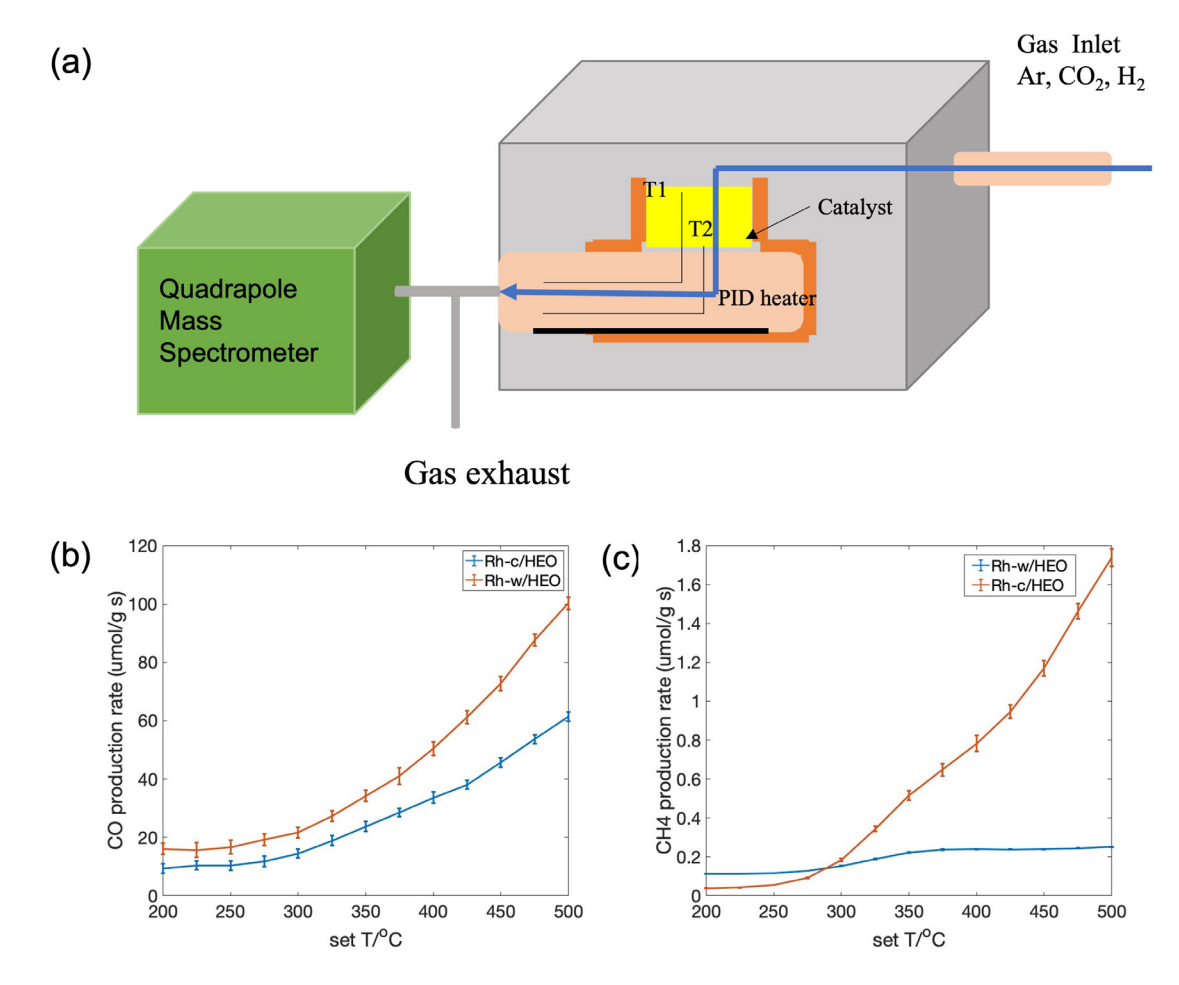


Figure 3: (a) CO2 hydrogenation solid-gas phase reaction system set-up; (b) Measured CO production rate, wet-impregnation method, Rh-w/HEO (blue curve), glycine-nitrate combustion method, Rh-c/HEO (red curve); (c) Measured CH4 production rate, wet-impregnation method, Rh-w/HEO (blue curve), glycine-nitrate combustion method, Rh-c/HEO (red curve)

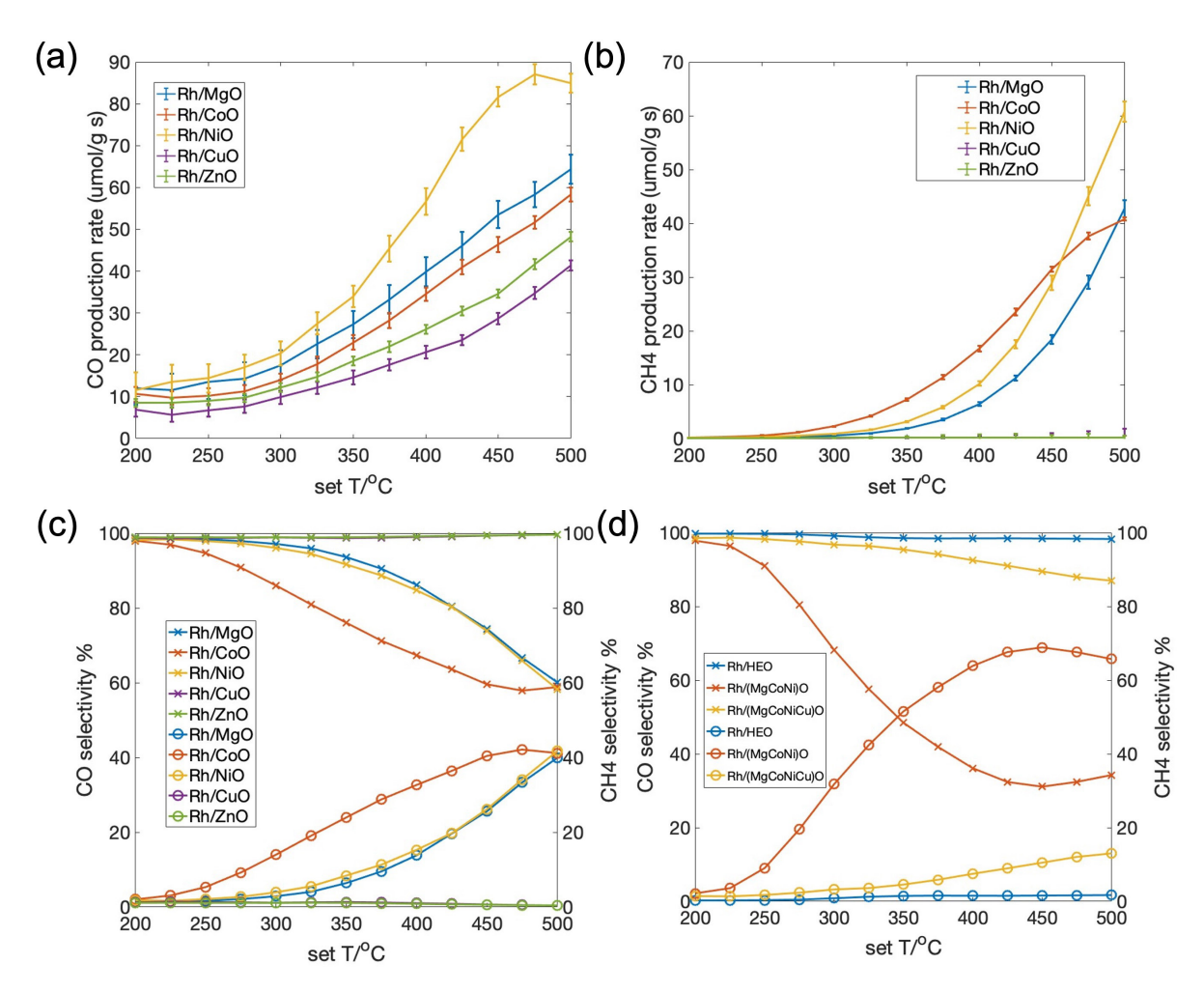


Figure 4: (a) Measured CO production rate, Rh/MgO (blue curve), Rh/CoO (red curve), Rh/NiO (yellow curve), Rh/CuO (purple curve), Rh/ZnO (green curve); (b) Measured CH4 production rate, Rh/MgO (blue curve), Rh/CoO (red curve), Rh/NiO (yel-low curve), Rh/CuO (purple curve), Rh/ZnO (green curve); (c) Calculated CO and CH4 selectivity, symbol 'x' corresponds to the CO selectivity on left y axis, symbol 'o' corresponds to the CH4 on right y axis, Rh/MgO (blue curve), Rh/CoO (red curve), Rh/NiO (yellow curve), Rh/CuO (purple curve), Rh/ZnO (green curve); (d) Calculated CO and CH4 selectivity, symbol 'x' corresponds to the CO selectivity on left y axis, symbol 'o' corresponds to the CH4 on right y axis, Rh/HEO (blue curve), Rh/(MgCoNiO) (red curve), Rh/(MgCoNiCu)O (yellow curve).

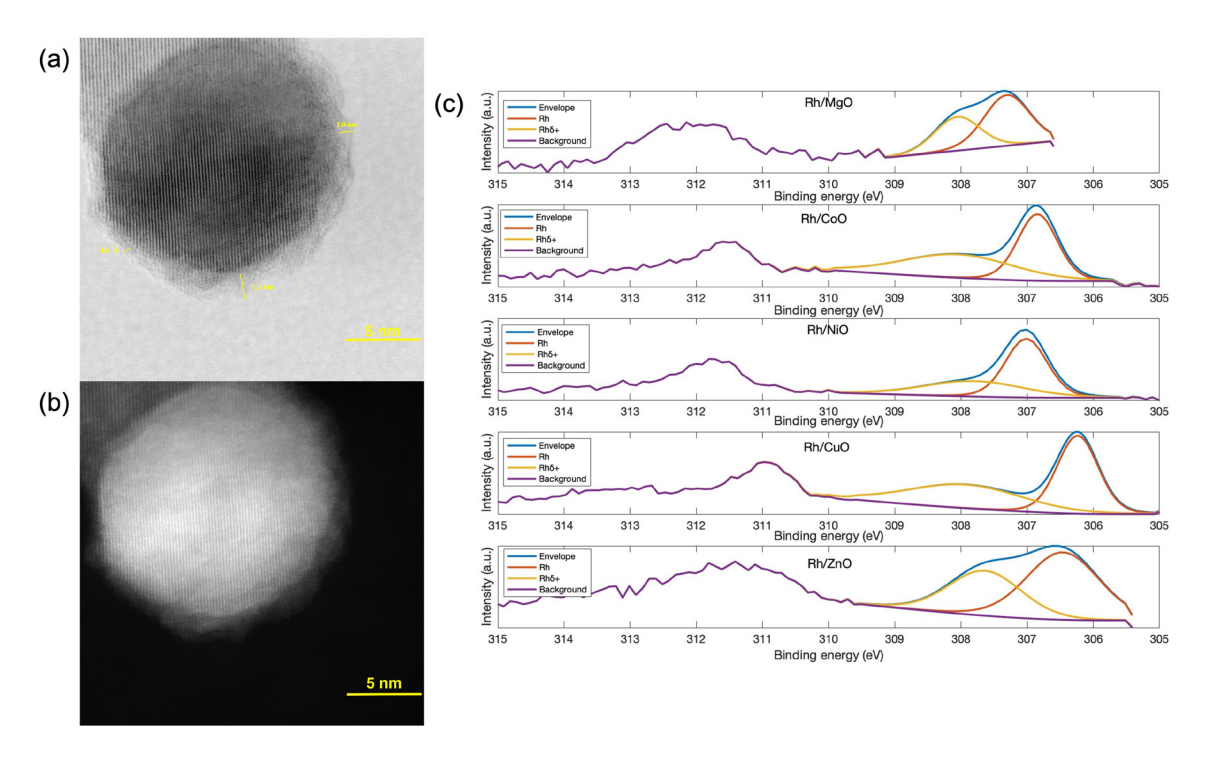


Figure 5: (a) High resolution STEM image for used Rh-c/HEO catalysts; (b) High resolution STEM image in HAADF mode for used Rh-c/HEO catalysts; (c)Rh 3d5/2 XPS spectra from all five single metal oxide catalysts. Envelope (blue curve), Rh^0 (red curve), $Rh^{\delta+}$ (yellow curve), background (purple curve).

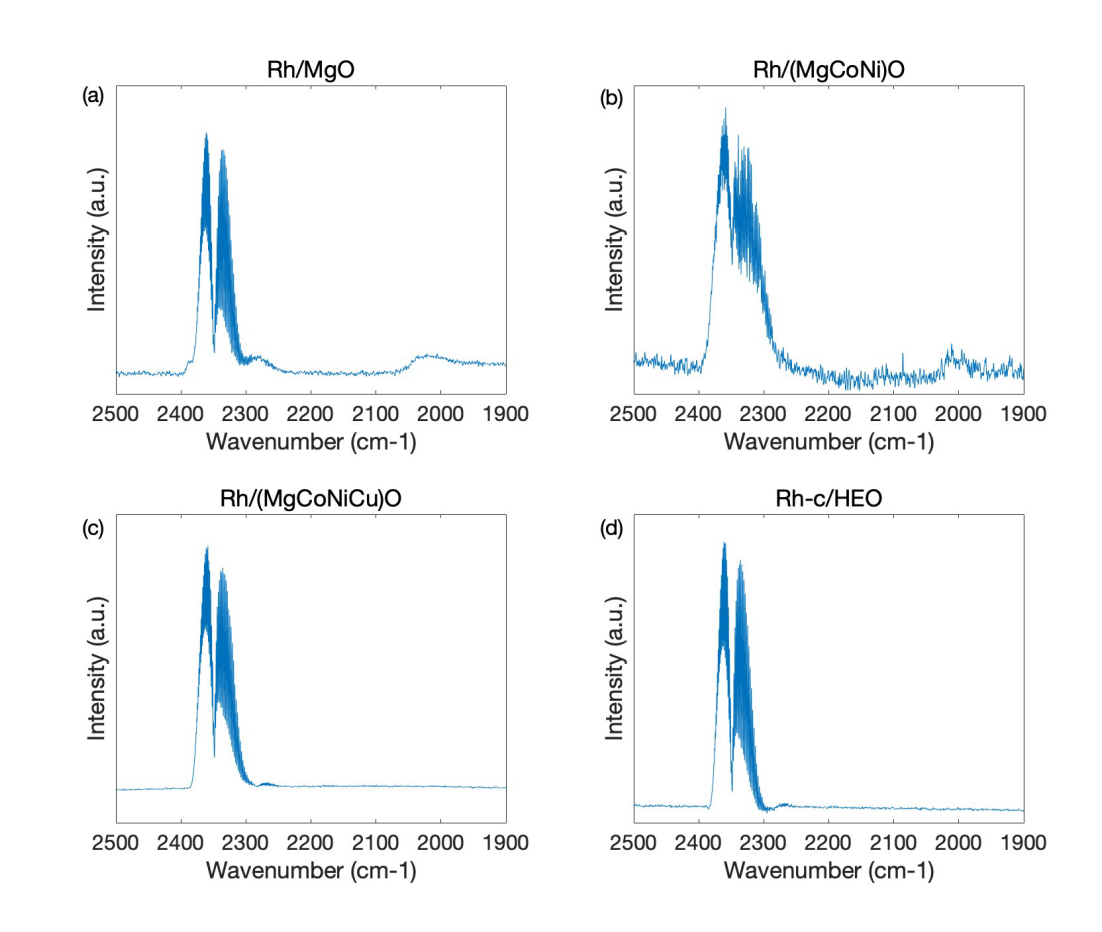


Figure 6: in situ DRIFTS spectra of (a) Rh/MgO, (b) Rh/(MgCoNi)O, (c) Rh/(MgCoNiCu)O and (d) Rh-c/HEO.